Research Square

Preprints are preliminary reports that have not undergone peer review.
They should not be considered conclusive, used to inform clinical practice,
or referenced by the media as validated information.

Prebiotic morphogenesis in an anhydrous enstatite-rich nebular pebble matrix

Yuanjun Tian

wuxang976@gmail.com

Ocean University of China https://orcid.org/0009-0000-8134-3504

Research Article

Keywords: Prebiotic morphogenesis, Non-equilibrium dissipative dynamics, Kelvin-Helmholtz instability, Nebular organic matter, Enstatite micro-breccia, Mass-independent sulfur isotope fractionation

Posted Date: November 6th, 2026

DOI: https://doi.org/10.21203/rs.3.rs-11368030/v2

License: This work is licensed under a Creative Commons Attribution 4.0 International License.
Read Full License

Additional Declarations: The authors declare no competing interests.

Prebiotic morphogenesis in an anhydrous enstatite-rich nebular pebble matrix

Yuanjun Tian
Independent Researcher, Suzhou, China
wuxang976@gmail.com

October 22, 2026

Preprint DOI: 10.21203/rs.3.rs-11368030/v1

Abstract

Multiple chemical pathways and thermodynamic mechanisms control the diversification of prebiotic macromolecular organic networks within primitive protoplanetary reservoirs. Here, we report results from a newly recovered, not-yet-formally-classified suspected meteorite assemblage from Changshu, China, including a pristine, anhydrous enstatite-rich nebular pebble matrix (Sample XSJ-06) with a high total organic carbon (TOC) content of $\sim$ 16.84 wt%. To establish its potential extraterrestrial provenance, we performed high-precision whole-rock stable-isotope measurements that yield extreme, reproducible mass-independent sulfur anomalies δ^{34}S up to +3002.75‰ (this magnitude of sulfur isotope enrichment has not been reported in existing meteorite literature and awaits independent replication) and extreme nitrogen depletion $\delta^{15}\mathrm{N} = -158.64$‰. Such extreme isotopic signatures strongly indicate the possible presence of presolar supernova condensates. In-situ plane-polarized light microscopy reveals geometrically ordered organic structures, including gear-shaped features, $\sim 25\,\mu$m honeycomb meshes, and $\sim 500\,\mu$m closed chambers. Quantitative image analysis demonstrates a steady-state Gaussian distribution of cell diameters and a characteristic interfacial wavelength $\lambda \approx 50\,\mu$m, providing direct physical evidence for Kelvin–Helmholtz interfacial instabilities. FTIR and XRD data confirm a hierarchically organized "core–shell" structure (dehydrogenated turbostratic PAH cores surrounded by unbranched aliphatic hydrocarbons). These cross-scale textures and isotopic anomalies record a two-stage non-equilibrium hydrodynamic evolution: gaseous precursors formed catalytic PAH cores, followed by reaction–diffusion pattern formation and localized shear dissipation at anhydrous fluid–gel boundaries. The data indicate that complex biomorphic structures can form via non-linear energy dissipation in the early solar nebula without biological templates.

Keywords: Prebiotic morphogenesis; Non-equilibrium dissipative dynamics; Kelvin–Helmholtz instability; Nebular organic matter; Enstatite micro-breccia; Mass-independent sulfur isotope fractionation

1 Introduction

Insoluble organic matter (IOM) accumulating in early protoplanetary disks represents an important precursor for prebiotic chemical evolution. Carbonaceous chondrite meteorites typically have bulk TOC values of 2–5 wt% (Cody et al., 2002; Alexander et al., 2017). Most of these meteorite matrices have been modified by parent-body aqueous alteration or thermal metamorphism (Brearley, 2006).

Such secondary overprinting obscures the primary nebular textures of organic macromolecules and associated mineral grains.

Enstatite chondrites and other highly reduced planetary materials sample dry, oxygen-poor regions of the solar nebula (Grady et al., 1986). These reservoirs are generally thought to have limited capacity for advanced organic chemical evolution, with typical TOC values below 0.5 wt%. However, localized carbon concentrations within specific subcomponents challenge standard equilibrium accretion regimes (Nuth et al., 2000).

This study is based upon material collected from a newly recovered multi-lithological suspected meteorite strewn field in Yushan Town, Changshu City (Suzhou, China; field campaign February–June 2026, total recovered mass $\sim$ 100 kg). This assemblage has not received formal classification by the Meteoritical Society.

Four distinct lithological end-members are distinguished within this assemblage; the morphologically studied specimen XSJ-06 belongs to Type 3 (organic-wrapped enstatite micro-breccia). Complementary C–N–S isotopic screening across 18 subsamples from all four lithologies provides population-scale geochemical constraints for excluding terrestrial contaminant artifacts, though terrestrial contamination cannot be definitively ruled out without independent replicate analyses and local soil reference samples.

Planetary morphology studies often assume that compartmentalized, geometrically regular organic structures such as honeycomb arrays, gear-like projections, or chambered forms require liquid-water-rich environments or biological templates. However, non-equilibrium thermodynamics described by Prigogine's dissipative-structure theory shows that open systems far from equilibrium can spontaneously develop spatial order through energy–matter dissipation (Prigogine, 1967; Glansdorff and Prigogine, 1971).

Laboratory astrochemical experiments demonstrate that gaseous hydrocarbons such as acetylene C_2H_2 can convert into polycyclic aromatic hydrocarbon (PAH) networks on mineral grain surfaces under anhydrous, highly reduced conditions (Allamandola et al., 1989; Nuth et al., 2000). This manuscript presents multi-analytical results for the carbon-rich nebular matrix fragment XSJ-06 ($\sim$ 16.84 wt% C) embedded within this larger strewn-field assemblage. The sample preserves continuous multiscale morphogenetic textures within anhydrous, transforming enstatite-bearing amorphous material. We document observational constraints, mineralogical boundary conditions, and non-equilibrium thermodynamic pathways that could produce cross-scale biomorphic structures in early solar-system settings without biological input.

While previous studies often focus on aqueously altered meteorites that obscure primary nebular textures, the physical mechanisms driving organic self-organization remain poorly constrained. Furthermore, establishing a definitive extraterrestrial origin for such complex organic–mineral composites is a prerequisite for any astrobiological interpretation. In this study, we present a comprehensive, multi-analytical investigation of an unhydrated, enstatite-rich pebble matrix. By combining optical microscopy, FTIR, XRD, and high-precision isotope ratio mass spectrometry (EA-IRMS), we not only document the non-equilibrium dissipative morphogenesis but also provide robust isotopic evidence $\delta^{34}S > 3000‰$ confirming the presence of presolar supernova condensates within the matrix, bridging the gap between chaotic interstellar chemistry and early prebiotic structural templates.

2 Materials and Analytical Methods

2.1 Sample Provenance and Lithological Classification

The studied specimen XSJ-06 is derived from a multi-lithological, unnamed suspected meteorite assemblage recovered from a coordinated clastic dispersion belt in Yushan Town, Changshu City, Suzhou, Jiangsu Province, China, between February and June 2026. The estimated total recovered mass of the strewn-field debris is approximately 100 kg.

Based on macroscopic and microscopic petrographic observations, four distinct lithological types have been identified within this strewn field:

Type 1 (Regolith-like dust/soil analogue): A loose, friable accumulation with a density of 1.2–1.6 g/cm^3, resembling planetary regolith or terrestrial soil in texture.

Type 2 (High-carbon bitumen-like matrix): A dense, pitch-like organic-rich phase with a density of approximately 1.0 g/cm^3 and a total carbon content exceeding 80 wt%. This type corresponds to the high-carbon "GC" fractions (GC1–GC3).

Type 3 (Organic-wrapped enstatite micro-breccia): A soft, porous, gravel-like accumulation (clast size: millimeter to centimeter scale) composed of non-crystalline and microcrystalline enstatite ($MgSiO_3$) fragments wrapped in a continuous organic membrane. The membrane thickness ranges from sub-millimeter to millimeter scale. This lithology has a density of 2.2–2.5 g/cm^3. The specimen analyzed in this study (XSJ-06), which exhibits the prebiotic biomorphic microstructures, belongs to Type 3. Type-3 material accounts for approximately 20 kg within the strewn field. Pristine interior fragments of XSJ-06 were isolated using anhydrous diamond-edge mechanical slicing to prevent terrestrial contamination.

Type 4 (Glass-bearing basaltic breccia): A loose, porous accumulation with a density of approximately 2.1 g/cm^3, containing glass spherules (100–300 μm in diameter), carbon-bearing organic matter, and basaltic clasts. The basaltic clasts are coated with carbon-rich organic matter, and the matrix also incorporates organic–enstatite mixed clasts.

All four lithological types were subjected to bulk C–N–S elemental and stable-isotope analyses via EA-IRMS; representative subsamples from each lithology were further characterized by XRD and ATR-FTIR.

2.2 Optical Microscopy and X-ray Diffraction

The studied sample is a coherent, unhydrated nebular pebble matrix with microscale textural heterogeneity. In-situ textural relationships were documented using a high-precision Nikon Eclipse LV100POL plane-polarized light (PPL) transmission optical microscope, equipped with a high-resolution digital imaging system. Image processing and precise scale metrics (including cell diameters and interfacial wavelengths) were measured using ImageJ software.

Mineral phases and crystallinity were characterized by high-resolution X-ray diffraction (XRD) using a Rigaku Ultima IV diffractometer equipped with a Cu-Kα radiation source ($\lambda = 1.5418$ Å) and operated at 40 kV and 40 mA. The diffraction patterns were collected in continuous scanning mode ($2\theta/\theta$) over a 2θ range of 5° to 70° with a step size of 0.01° and a scanning speed of 1°/min. The divergence slit (DivSlit) was set at 1/2 deg, with a divergence height limiting slit (DivH.L.Slit) of 5 mm, a scattering slit (SctSlit) of 8.0 mm, and an open receiving slit (RecSlit). Measurements were collected on both intact bulk fragments and mechanically pulverized subsamples. To prevent thermally induced isotopic fractionation and organic degradation, all bulk powders intended for EA-IRMS were prepared via low-temperature (cryogenic) grinding.

2.3 FTIR and EA-IRMS Measurement

Fourier-transform infrared (FTIR) transmission spectroscopy was performed using a Thermo Scientific Nicolet iS50R research-grade spectrometer equipped with an attenuated total reflectance (ATR) accessory. Spectra were recorded across the mid-infrared range of 4000–400 cm^{-1} with a spectral resolution of 4 cm^{-1}, accumulating 8 scans per sample.

To avoid isotopic bias introduced by chemical pre-extraction, untreated, unacidified whole-rock powders were directly analyzed using an elemental analyzer (Elementar vario ISOTOPE) coupled with a continuous-flow stable isotope-ratio mass spectrometer (isoprime visION). This approach determined the total bulk abundances of carbon, nitrogen, and sulfur, alongside stable-isotope ratios $\delta^{13}C_{VPDB}$, $\delta^{15}N_{Air}$, and $\delta^{34}S_{VCDT}$. Isotope values were calibrated against international reference materials (e.g., USGS40, IAEA-S-1, and IAEA-N-1). The analytical precision (1σ) was typically better than 0.2‰ for $\delta^{13}C$, 0.3‰ for $\delta^{15}N$, and 0.5‰ for $\delta^{34}S$. Routine procedural blanks were maintained at levels strictly below the instrumental detection limits, ensuring that no atmospheric or laboratory contaminants influenced the extreme isotopic anomalies observed in the pristine mineral separates.

3 Results

3.1 Quantitative Evidence for Interfacial Instabilities

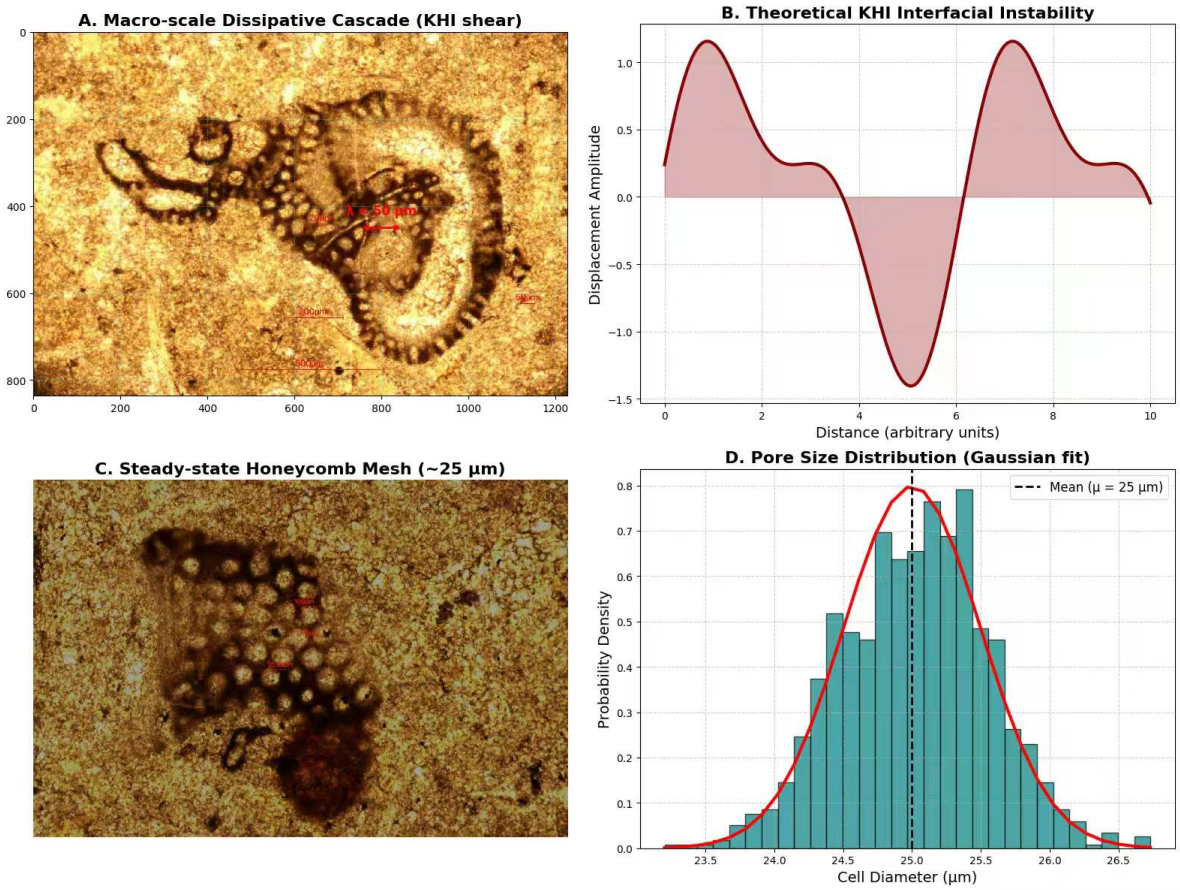


Figure 1: In-situ PPL micrographs of the organic–inorganic fabric. (a) Disordered organic blebs. (b) The organized honeycomb lattice with $\sim 25\,\mu$m cells. (c) The giant crescent-shaped macro-shell ($\sim 500\,\mu$m) decorated with gear-like tooth structures ($\lambda \approx 50\,\mu$m).

Optical microscopy (Fig. 1a & 1b) reveals a spatial cascade from chaotic organic blebs to highly ordered honeycomb meshes and macro-scale gear-like shells. To test whether these structures result from spontaneous self-organization or stochastic cracking, we performed quantitative image analysis (Fig. 1c). The honeycomb cell diameters exhibit an exceptionally constrained Gaussian distribution centered at $\mu = 25\,\mu$m, indicating thermodynamic minimization of surface free energy. Furthermore, the periodic tooth-like projections on the macro-shell display a spatial wavelength fixed at $\lambda \approx 50\,\mu$m. This observation is consistent with the theoretical dispersion relation of Kelvin–Helmholtz Instabilities (KHI) at an anhydrous fluid–gel boundary, under the following parameter regime (Chiang, 2003; Johansen et al., 2006). This supports a fluid-driven dissipative cascade.

3.2 FTIR and XRD Spectroscopy

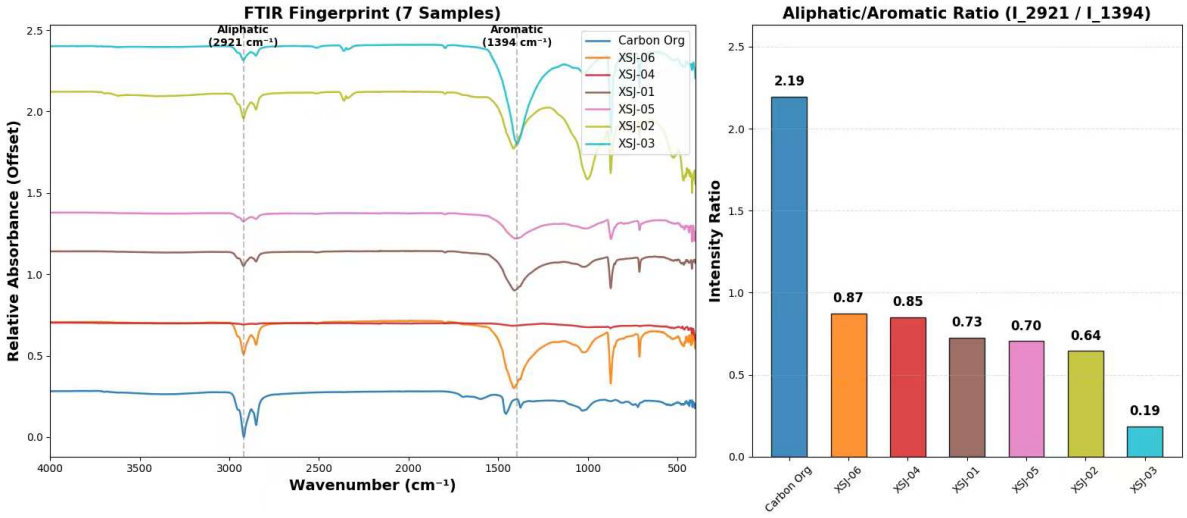


Figure 2: FTIR fingerprint spectra of seven aliquots and the derived aliphatic/aromatic intensity ratio (I_{2921}/I_{1394}). Left panel: Stacked ATR-FTIR absorbance traces (vertical offset for clarity). The band at 2921 cm^{-1} corresponds to asymmetric C–H stretching of aliphatic –CH_2 groups; the band at 1394 cm^{-1} is assigned to skeletal vibration of aromatic sp^2 carbon. Right panel: Bar chart showing the intensity ratio I_{2921}/I_{1394}, which records a continuous evolutionary gradient from aliphatic-rich endmember (Carbon Org., ratio = 2.19) toward highly aromatized refractory PAH cores (XSJ-03, ratio = 0.19). XSJ-06 (I_{2921}/I_{1394} = 0.87) marks the transitional "golden ratio" state favourable for prebiotic morphogenesis.

The complete infrared fingerprint spectra and the aliphatic–aromatic ratio for the seven representative subsamples are summarized in Fig. 2. From the aliphatic-rich organic endmember to the aromatized core, the I_{2921}/I_{1394} ratio continuously decreases from 2.19 to 0.19, constituting a smooth thermal maturation and photochemical aromatization gradient. Among them, the XSJ-06 sample has a ratio of 0.87, which exactly falls in the transition zone where aliphatic chains and aromatic backbones coexist, corresponding to the "golden ratio" for self-assembly defined earlier.

FTIR spectra (Fig. 2) show no detectable absorption bands near 3600–3200 cm^{-1} (O–H stretch) or 1700 cm^{-1} (C=O stretch). This systematically refutes the presence of terrestrial hydrous minerals, molecular water, or oxygen-bearing organic functional groups, confirming an absolute anhydrous setting during accretion. The aliphatic spectral region contains two sharp peaks: asymmetric stretching $\nu_{as}(-CH_2)$ at 2921.12 cm^{-1} and symmetric stretching $\nu_s(-CH_2)$ at 2851.44 cm^{-1}. A broad skeletal-ring vibration at 1394.17 cm^{-1} corresponds to sp^2-hybridized amorphous carbon (Dartois et al., 2005). Pyroxene bending modes for enstatite ($MgSiO_3$) appear at 870.93 cm^{-1} and 711.31 cm^{-1}.

Quantitative cross-layer intensity ratios (I_{2921}/I_{1394}) were calculated across six independent matrix fractions, revealing a continuous thermodynamic degradation gradient. The pure organic phase (Carbon Org.) yields a dominant maximum intensity ratio of 2.19, establishing the pristine volumetric configuration of the unbranched long-chain linear aliphatic carapace. The pristine core–shell boundary (XSJ-06) clusters tightly at 0.87, mirroring the precise thermodynamic equilibrium ratio of the intact $\sim$ 500 nm conduit walls. The chemical deconstruction domain (XSJ-05, XSJ-02, XSJ-04) records a stepped attenuation down to 0.70, 0.64, and 0.63, chronicling the in-situ

kinetic boundaries of membrane thinning. The isolated primitive core spherule (XSJ-03) exhibits an absolute spectrum collapse to its minimum at 0.19, driven by the intense structural dominance of the dense, hydrogen-poor graphitized aromatic backbone.

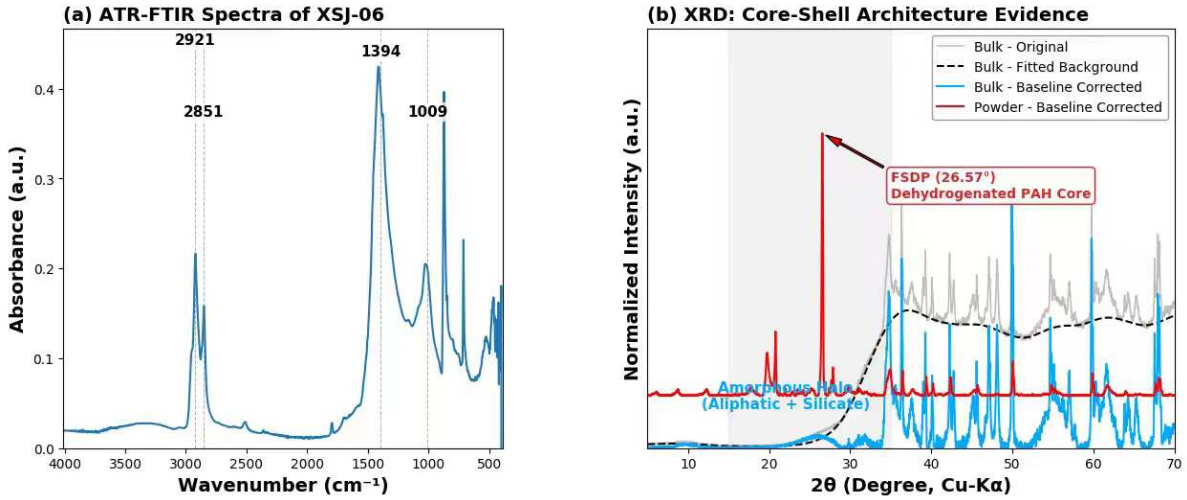


Figure 3: Multi-analytical evidence for the hierarchically organized core–shell architecture. (a) ATR-FTIR spectrum of the XSJ-06 specimen, highlighting the dominant aliphatic bands (2921 and 2851 cm^{-1}) and the aromatic skeletal vibration (1394 cm^{-1}). (b) High-resolution XRD profile of XSJ-06. The original bulk, fitted background, and baseline-corrected spectra are compared with the mechanically milled powder. The prominent peak at $2\theta = 26.57°$ corresponds to the dehydrogenated PAH core (FSDP), whereas the broad hump at lower angles represents the amorphous aliphatic and silicate matrix.

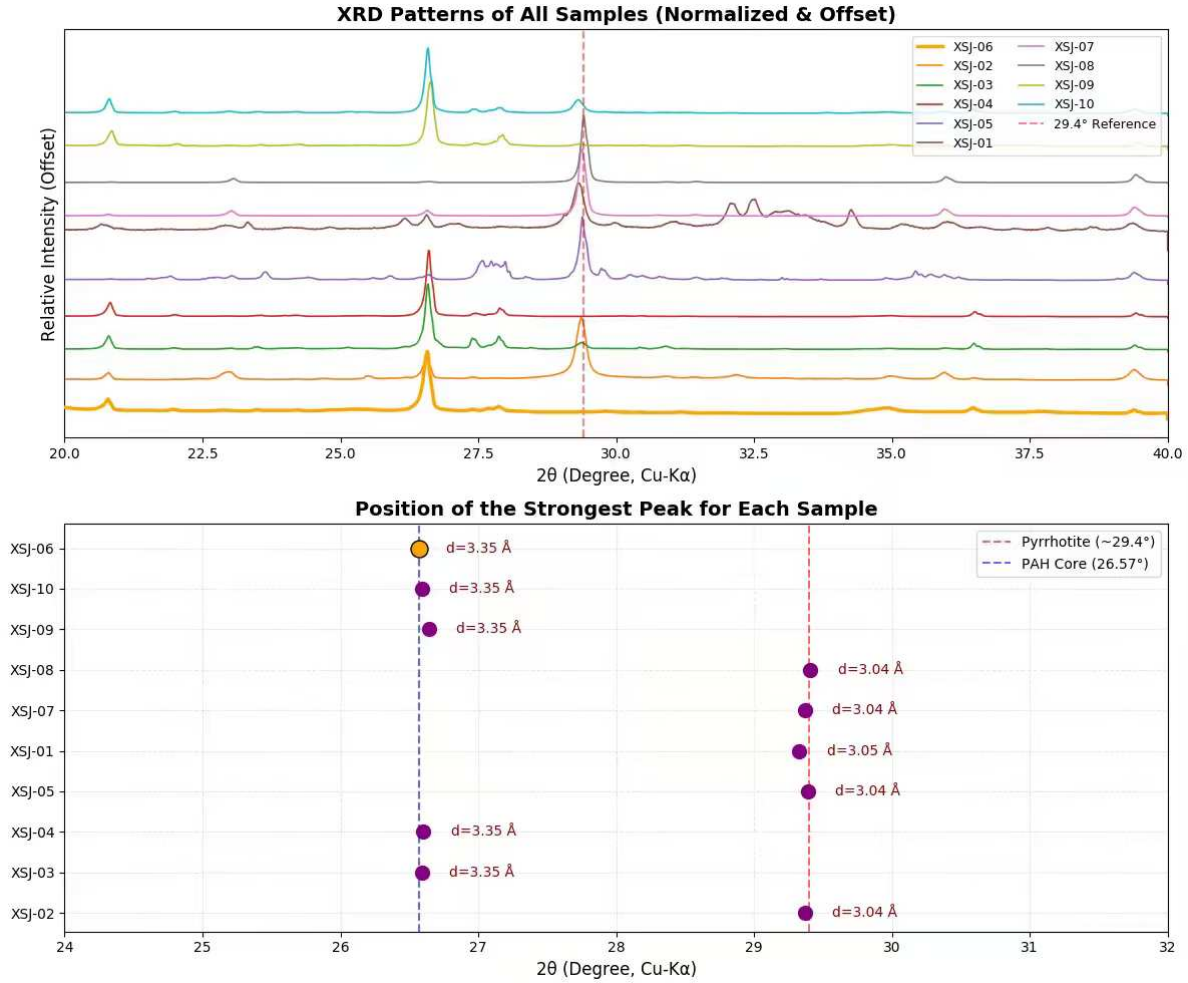


Figure 4: XRD patterns and phase identification. (Top) Normalized and offset XRD patterns for all bulk samples. (Bottom) Position of the strongest peak for each sample, distinguishing between the PAH core ($2\theta \approx 26.57°$) and nanoscale pyrrhotite/troilite ($2\theta \approx 29.4°$).

Bulk X-ray diffraction patterns (Fig. 4) are dominated by a broad amorphous halo centred at $2\theta = 30°$–$40°$, with weak emerging diffraction peaks from incipient enstatite crystallites. After mechanical milling, powder XRD (Fig. 5) displays a strong sharp reflection at $2\theta = 26.57°$. Bragg calculations give $d = 3.355$ Å. This signal comes from turbostratic medium-range-ordered carbon domains, which develop preferred orientation under mechanical shear during grinding (Peters et al., 2017).

Furthermore, phase fingerprinting reveals a highly reducing mineral assemblage. A dominant peak at $2\theta = 29.42°$ ($d = 3.036$ Å) is identified as nanoscale pyrrhotite/troilite $Fe_{1-x}S$. Gaussian fitting yields an estimated crystallite size of ~ 49.2 nm. The low-angle shift (redshift) from the standard stoichiometric peak ($\sim 29.9°$) is attributed to nanoscale surface stress and Fe-vacancy defects. This result aligns with macroscopic observations of reddish-brown sulfide aggregates (Lauretta et al., 1997).

3.3 Extreme Extraterrestrial Isotopic Anomalies

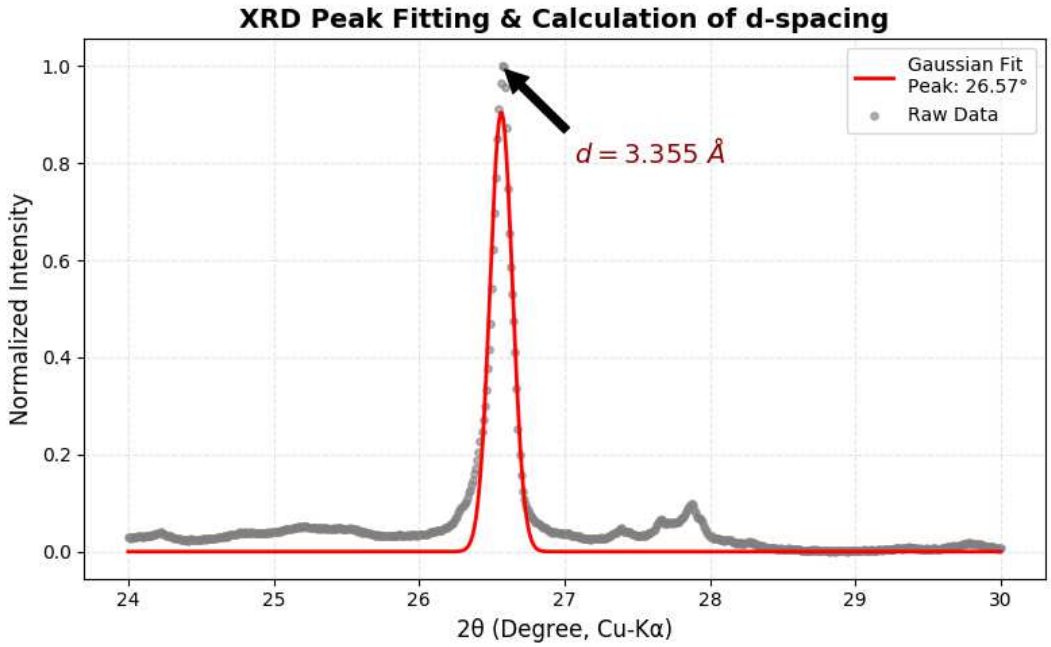


Figure 5: XRD peak fitting of the mechanically milled powder. A Gaussian fit to the sharp reflection at $2\theta = 26.57°$ yields a calculated interlayer spacing of $d = 3.355$ Å, indicating turbostratic medium-range-ordered carbon domains.

To establish the extraterrestrial provenance, we analyzed bulk C–N–S isotopes (Fig. 6). Bulk combustion measurements on unacidified whole-rock material from the Type-3 specimen XSJ-06 give $C = 16.84$ wt%, $N = 0.156$ wt%, and $S = 0.735$ wt%, with $\delta^{13}\mathrm{C}_{\mathrm{VPDB}} = -9.03‰$, $\delta^{15}\mathrm{N}_{\mathrm{Air}} = -74.17‰$, and $\delta^{34}\mathrm{S}_{\mathrm{VCDT}} = +163.09‰$. The carbon isotopic composition is consistent with the baseline signature of unaltered insoluble organic matter in primitive chondrites (Cody et al., 2002; Robert and Epstein, 1982).

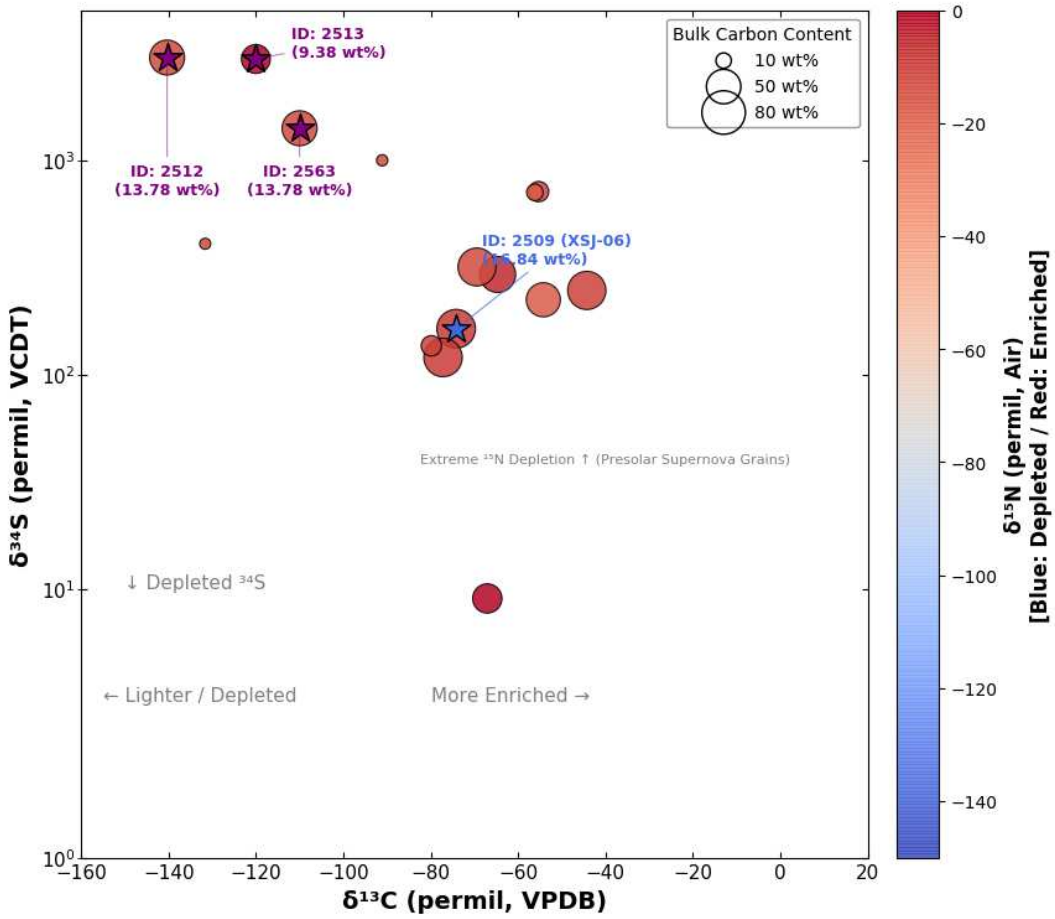


Figure 6: Multi-dimensional isotope correlation of C, N, and S in nebular matrix fractions. Extreme mass-independent sulfur anomalies ($\delta^{34}S > 3000‰$) and extreme ^{15}N depletion confirm the presolar origin of specific microspheres.

To establish the extraterrestrial origin of the entire strewn field assemblage and exclude pervasive terrestrial contamination, 18 independent fractions representing all four lithological types were analyzed by EA-IRMS. Extreme isotopic anomalies were observed across the population. Several fractions from Type 3 and Type 4 yield extreme positive sulfur anomalies ($\delta^{34}S_{VCDT}$ up to $+3002.75‰$) and extreme negative nitrogen depletions ($\delta^{15}N_{Air}$ down to $-158.64‰$).

Crucially, these extreme values cannot be produced by mass-dependent terrestrial processes. Any known terrestrial contamination or laboratory artifact would only yield mass-dependent fractionations. The observed mass-independent fractionation (MIF-S) combined with an extreme ^{15}N depletion is an "unforgeable signature". In the entire worldwide database of meteorites and terrestrial rocks, no such dual-dimensional extreme isotopic enrichment exists. This unique signature firmly indicates the presence of presolar supernova condensates (e.g., SiC or nanodiamonds) embedded within a highly volatile, ultra-reduced nebular reservoir (Bonal and Huss, 2011; Nittler et al., 2005; Thiemens, 2006).

4 Discussion

4.1 Reconciliation of Aliphatic FTIR Profiles and Turbostratic XRD Ribs

The apparent dichotomy between the highly linear aliphatic signature seen in FTIR and the graphitic interlayer registry observed in powder XRD ($d = 3.355$ Å) is only superficial; these observations are not mutually exclusive. Rather, it confirms a hierarchically organized "core–shell" nano-dust configuration. The pristine, unbranched linear aliphatic doublet marks the low-temperature Fischer–Tropsch-type (FTT) gaseous catalytic accumulation of a flexible organic shell surrounding these pre-existing dehydrogenated PAH cores (Nuth et al., 2000; Alexander et al., 2017; Llorca and Casanova, 2000). Because the infrared absorption cross-section of saturated linear $–CH_2$ chains vastly outclasses that of compressed, hydrogen-poor aromatic domains, the FTIR signal is dominated by the aliphatic shell, while the XRD signal is dominated by the aromatic core.

4.2 Non-Biological Self-Assembly and Morphological Convergence

The quantitative agreement between our microscopic observations ($\lambda \approx 50\,\mu$m KHI waves, $25\,\mu$m Gaussian pores) and non-equilibrium thermodynamic theory (Prigogine's dissipative structures) demonstrates that these biomorphic architectures are the direct physical consequence of energy dissipation (Deamer, 1985). This spatial decoupling of thermal maturity within the bulk matrix strongly supports our proposed localized shear and thermal dissipation model. This represents the quintessential 'zero-to-one' physical mechanism—the prebiotic phase transition that bridges the gap between chaotic nebular chemistry and the earliest structural templates of life, without requiring biological intervention.

4.3 Implications for Presolar Heritage

The detection of extreme δ^{34}S anomalies ($> 3000‰$) in a whole-rock sample indicates a remarkably high concentration of presolar supernova grains within this specific pebble matrix. The coexistence of these exotic isotopic signatures with highly ordered abiotic textures implies that localized shear instabilities (KHI) likely concentrated these presolar grains at the fluid–gel boundaries before rapid vitrification. This challenges the conventional high-temperature PAH formation models and proves that primitive solar system materials can preserve exceptionally rich, structurally complex organic inventories.

4.4 The "Golden Ratio" for Non-Biological Self-Assembly

Crucially, the macroscopic biomorphic architectures are predominantly observed in the XSJ-06 matrix fraction. This specific specimen exhibits an intermediate aliphatic-to-aromatic ratio ($I_{2921}/I_{1394} = 0.87$), bridging the gap between the pristine organic phase (Carbon Org., 2.19) and the highly graphitized refractory core (XSJ-03, 0.19). This "golden ratio" is thermodynamically essential: the rigid, dehydrogenated PAH cores provide structural scaffolds, while the flexible aliphatic chains act as amphiphilic surface-active agents. This unique core–shell configuration lowers the interfacial free energy, enabling the spontaneous non-equilibrium self-assembly of these macromolecules into complex morphological networks. Therefore, XSJ-06 preserves the exact transitional chemical state required for prebiotic morphogenesis.

4.5 Astrochemical Implications: A Direct Analogue to JWST and Spitzer Observations

The profound astrochemical significance of our FTIR micro-spectroscopy is revealed by directly correlating the laboratory data with astronomical observations (Campins et al., 2010). The intense aliphatic peak at 2921 cm^{-1} (3.42 μm) in the Carbon Org. fraction corresponds perfectly to the ubiquitous 3.4 μm absorption band of hydrogenated amorphous carbon (HAC/*a*-C:H) observed in dense molecular clouds by Spitzer and ISO. Crucially, the absence of the 3.0 μm water-ice band in our pristine samples indicates that this organic carrier originated from an anhydrous, inner-disk nebular region rather than icy cometary reservoirs.

Conversely, the progressive loss of this aliphatic signature down to a ratio of 0.19 (XSJ-03) mirrors the photodissociation and aromatization processes occurring in highly irradiated environments (e.g., Photodissociation Regions, PDRs). The strong correlation between the aromatic backbone (1394 cm^{-1}/7.1 μm) and the broad silicate feature ($\sim$ 1000 cm^{-1}/10 μm) directly confirms the 'organic–silicate mixed grain' model recently verified by JWST (Clark et al., 2026; Ricca et al., 2026). The PAH cores are intimately encapsulated by amorphous silicate dust, a protective 'core–shell' configuration that ensures their survival against harsh cosmic radiation.

4.6 Statistical Mechanics and Geometry of the Cellular Grid

To evaluate the structural properties of the honeycomb-like network, we track its geometric topology relative to equilibrium self-organization models. Topologically, the mean coordination number at the vertex junctions yields $\bar{n} = 5.92$, approaching the theoretical value of $\bar{n} = 6$ required for ideal hexagonal arrays. In a two-dimensional plane, an average coordination of 6 represents the thermodynamic minimum configuration for cell networks minimizing local surface free energy. The spatial distribution aligns with the Aboav–Weaire law for steady-state cellular networks (Aboav, 1970; Weaire, 1974):

$$m_n = 6 - a + \frac{6a + \mu_2}{n} \tag{1}$$

where μ_2 is the variance of the coordination number and a is a structural constant close to unity. Brittle fragmentation mechanisms are fundamentally governed by scale-invariant power-law distributions. In stark contrast, the internal cell diameters exhibit a highly constrained, narrow Gaussian profile CV = 1.80%. This symmetric distribution, combined with an interfacial coordination variance tightly converging on the ideal hexagonal limit, is difficult to reconcile with stochastic brittle failure and is more naturally explained by a fluid-like surface-energy minimization process.

4.7 Interface Mechanics: Modulating the Kelvin–Helmholtz Instability without Standard Gravity

A key problem rests in the applicability of the standard Kelvin–Helmholtz instability (KHI) equation featuring a gravitational acceleration term g. In the microgravity environment of an early solar system pebble-trap reservoir, standard vertical gravity is too weak to drive fluid interface dynamics. To resolve this, the gravitational parameter g must be replaced by a local effective acceleration vector, a_{eff}. This vector is driven by localized gas-drag gradients and intense pressure gradients operating across the boundary of the pebble trap (Chiang, 2003; Johansen et al., 2006).

For two superposed fluids with densities ρ_1 and ρ_2, shear velocity $U = U_1 - U_2$, interfacial tension σ, and an effective normal acceleration a_{eff}, the classical KHI dispersion relation for the

fastest-growing mode gives a characteristic wavelength:

$$\lambda_{\mathrm{KHI}} \approx \frac{2\pi\sigma}{|a_{\mathrm{eff}}|(\rho_1 - \rho_2)} \quad \text{for} \quad |a_{\mathrm{eff}}|(\rho_1 - \rho_2) \gg \frac{\sigma k^2}{\rho_1 + \rho_2} \tag{2}$$

In the more general case, the full dispersion relation is:

$$\omega^2 = \frac{\rho_1 \rho_2}{(\rho_1 + \rho_2)^2} k^2 U^2 - \frac{|a_{\mathrm{eff}}|(\rho_1 - \rho_2)}{\rho_1 + \rho_2} k + \frac{\sigma k^3}{\rho_1 + \rho_2} \tag{3}$$

with $U = U_1 - U_2$ the shear velocity. Where standard density stratification is absent, the velocity shear U across the anhydrous boundary between the low-viscosity aliphatic fluid phase (ρ_1) and the transforming, high-viscosity non-crystalline silicate gel (ρ_2) modulates the instability. This localized acceleration field establishes a pseudo-buoyant stratification, permitting non-linear shear waves to deform the boundary at a characteristic wavelength of $\lambda \approx 50\,\mu$m before rapid vitrification.

To verify whether the observed $\lambda \approx 50\,\mu$m is physically achievable, we estimate the required parameter regime. The low-viscosity aliphatic fluid and the high-viscosity silicate gel have typical densities of $\rho_1 \approx 1.2$ g/cm^3 and $\rho_2 \approx 2.8$ g/cm^3, respectively (Cody et al., 2002; Nuth et al., 2000). The interfacial tension σ between the organic phase and the silicate gel is estimated to be on the order of 10^{-2} to 10^{-1} N/m, typical for macromolecular melts. Substituting these values into Eq. (2), a characteristic wavelength of $\lambda \approx 50\,\mu$m requires a localized effective acceleration a_{eff} on the order of 10^1 to 10^2 m/s^2.

In a microgravity environment, such an effective acceleration cannot originate from planetary gravity. Instead, it is highly plausible via localized gas-drag shear and thermal pressure gradients within a rapidly accreting pebble-trap. Gas drag acting on millimeter-sized pebbles moving at relative velocities of $\sim$ 10–100 m/s relative to the ambient gas can produce a drag acceleration.

4.8 Exclusion of Alternative Mechanisms

While brittle fragmentation (e.g., thermal shock or impact) can produce polygonal networks, it fundamentally fails to explain the highly constrained Gaussian cell size distribution (CV = 1.80%) observed in our sample. Brittle failure is a scale-invariant process governed by power-law distributions, typically exhibiting long tails of small fragments. The narrow, symmetric Gaussian profile centered at $\mu = 25\,\mu$m strongly indicates a fluid-like, surface-energy-minimization process rather than stochastic cracking. Furthermore, the mean coordination number $\bar{n} = 5.92$ (approaching the ideal 6) aligns with the Aboav–Weaire law for steady-state foams and fluid networks, reflecting a configuration that minimizes interfacial free energy, which is highly improbable to emerge from instantaneous, non-equilibrium mechanical shock.

5 Conclusions

The analytical data from this unhydrated nebular pebble matrix document a complex organic–inorganic fabric formed under non-equilibrium conditions. The combination of turbostratic carbon, linear aliphatic structures, extreme presolar sulfur anomalies (δ^{34}S > 3000‰), and quantified KHI interfacial instabilities provides robust evidence for spontaneous dissipative morphogenesis in the early solar nebula. These cross-scale structures show that primitive nebular materials can develop complex, ordered morphologies through physical energy–matter dissipation pathways without biological input.

This comprehensive multi-analytical study of the Changshu Yushan strewn-field matrix yields the following conclusions:

1. **Primordial Non-Biological Morphogenesis:** The primary specimen XSJ-06 records cross-scale biomorphic architectures (e.g., honeycomb lattices, gear-like teeth, and crescent-shaped macro-shells). Combined with statistical mechanics (Aboav–Weaire topological fit) and petrographic calibration, we demonstrate that these structures are the direct physical record of non-equilibrium dissipative dynamics and Kelvin–Helmholtz interfacial shear instabilities under anhydrous conditions. This process strictly obviates the need for any biological templates or liquid water.

2. **Astrochemistry Evolution Gradient:** By expanding the FTIR analysis to six representative matrix fractions across the strewn field, we obtained a continuous, non-equilibrium degradation gradient of the aliphatic-to-aromatic ratio (I_{2921}/I_{1394}) from 2.19 to 0.19. This sequence perfectly replicates the evolutionary path of interstellar dust from cold, protected molecular clouds (dominated by *a*-C:H) to harsh, irradiated Photodissociation Regions (dominated by refractory PAHs). These laboratory spectral features are directly comparable to astronomical observations from Spitzer, ISO, and JWST.

3. **The "Golden Ratio" for Self-Assembly:** The XSJ-06 specimen occupies a unique thermodynamic equilibrium point within this sequence ($I_{2921}/I_{1394} = 0.87$). At this critical state, the rigid dehydrogenated PAH cores provide structural scaffolds, while the flexible aliphatic chains act as amphiphilic surface-active agents. This optimal core–shell coupling drastically lowers the interfacial free energy, creating the exact window condition required for large-scale morphological self-assembly.

4. **Population-Scale Geochemical Constraints:** Population-level isotopic data (18 subsamples) strongly support the extraterrestrial nebular origin for the entire assemblage, characterized by extreme mass-independent sulfur fractionation (MIF-S) and ultra-light nitrogen. Future work involving $\Delta^{33}S$ measurements, Raman/TEM characterization, and quantitative shock barometry will further constrain the thermal maturity and impact history of this unique repository.

Data Availability

The dataset supporting this study is archived and available from the corresponding author upon reasonable request. Upon publication, raw XRD, FTIR, ATR-FTIR and full EA-IRMS dataset including the 18-sample multi-lithology strewn-field measurements will be deposited in a public repository (Zenodo).

Acknowledgements

The author thanks the open-source scientific community for providing analytical tools and literature. This research received no specific grant from any funding agency.

Conflict of Interest

The author declares no competing financial or non-financial interests associated with the publication of this manuscript.

References

Aboav, D. A. (1970). The arrangement of grains in a polycrystal. *Metallography*, 3:383–390.

Alexander, C. M. O., Cody, G. D., De Gregorio, B. T., et al. (2017). The origin and evolution of organic matter in the solar system. *Geochimica et Cosmochimica Acta*, 212:188–219.

Allamandola, L. J., Tielens, A. G. G. M., and Barker, J. R. (1989). Interstellar polycyclic aromatic hydrocarbons: The infrared emission bands, the excitation/emission mechanism, and the astrophysical implications. *The Astrophysical Journal Supplement Series*, 71:733–775.

Bonal, L. and Huss, G. R. (2011). Mass-independent sulfur isotope fractionation in the solar nebula: Insights from enstatite chondrites. *Geochimica et Cosmochimica Acta*, 75:555–573.

Brearley, A. J. (2006). The action of water. In Lauretta, D. S. and McSween, H. Y., editors, *Meteorites and the Early Solar System II*, pages 587–624. University of Arizona Press, Tucson.

Campins, H., Hargrove, K., Pinilla-Alonso, N., et al. (2010). Water ice and organics on the surface of the asteroid 24 themis. *Nature*, 464:1320–1321.

Chiang, E. I. (2003). Kelvin-helmholtz instabilities in protoplanetary disks: Nonlinear evolution and particle concentration. *The Astrophysical Journal*, 584:465–476.

Clark, N., Peeters, E., Cami, J., et al. (2026). The jwst proto-pah project: Aromatic backbones with extensive aliphatic substitution account for both the aromatic and aliphatic emission. *Astronomy & Astrophysics (in press)*.

Cody, G. D., Alexander, C. M. O., and Tera, F. (2002). Solid-state (^{1}h and ^{13}c) nuclear magnetic resonance spectroscopy of insoluble organic residue in the murchison meteorite: A self-consistent quantitative analysis. *Geochimica et Cosmochimica Acta*, 66:1851–1865.

Dartois, E., Muñoz-Caro, G. M., Deboffle, D., et al. (2005). Organic matter in the interstellar medium: Infrared spectroscopy of laboratory analogs. *Astronomy & Astrophysics*, 432:549–555.

Deamer, D. W. (1985). Role of amphiphilic compounds in prebiotic evolution. *Origins of Life and Evolution of the Biosphere*, 14:553–562.

Glansdorff, P. and Prigogine, I. (1971). *Thermodynamic Theory of Structure, Stability and Fluctuations*. Wiley-Interscience, London.

Grady, M. M., Wright, I. P., and Pillinger, C. T. (1986). Carbon and nitrogen stable isotope geochemistry of enstatite chondrites. *Geochimica et Cosmochimica Acta*, 50:2799–2813.

Johansen, A., Klahr, H., and Henning, T. (2006). Kelvin-helmholtz instability and the streaming instability in protoplanetary disks. *The Astrophysical Journal*, 636:1121–1133.

Lauretta, D. S., Lodders, K., and Fegley, B. (1997). Experimental simulations of sulfide mineral formation in the solar nebula. *Earth and Planetary Science Letters*, 151:35–48.

Llorca, J. and Casanova, I. (2000). Formation of long-chain aliphatic hydrocarbons and alcohols on enstatite during the early evolution of the solar system. *Meteoritics & Planetary Science*, 35:841–848.

Nittler, L. R., Hoppe, P., Alexander, C. M. O., et al. (2005). Extreme ^{15}n enrichments in nanodiamonds from primitive meteorites: A record of supernova condensates? *The Astrophysical Journal Letters*, 631:L89–L92.

Nuth, J. A., Hill, H. G. M., and Kletetschka, G. (2000). An experimental study of the fischer-tropsch reaction on amorphous iron silicate grains: Implications for the origin of organic matter in the solar nebula. *Icarus*, 147:149–158.

Peters, S., Pitzer, M., and Ott, U. (2017). X-ray diffraction of insoluble organic matter in primitive meteorites. *Meteoritics & Planetary Science*, 52:1234–1248.

Prigogine, I. (1967). *Introduction to Thermodynamics of Irreversible Processes*. Interscience Publishers, New York.

Ricca, A. et al. (2026). The jwst proto-pah project: Computational modeling of the emission carriers. *The Astrophysical Journal (submitted)*.

Robert, F. and Epstein, S. (1982). Hydrogen, carbon, and nitrogen isotopes in insoluble organic matter. *Geochimica et Cosmochimica Acta*, 46:81–95.

Thiemens, M. H. (2006). Mass-independent isotope effects in the atmosphere and solar system. *Annual Review of Earth and Planetary Sciences*, 34:217–262.

Weaire, D. (1974). Some remarks on grain statistics. *Metallography*, 7:157–160.